This paper is published as part of a PCCP Themed Issue on:

Modern EPR Spectroscopy: Beyond the EPR Spectrum

Guest Editor: Daniella Goldfarb

Editorial

Modern EPR spectroscopy: beyond the EPR spectrum
Phys. Chem. Chem. Phys., 2009
DOI: 10.1039/b913085n

Perspective

Molecular nanomagnets and magnetic nanoparticles: the EMR contribution to a common approach
M. Fittipaldi, L. Sorace, A.-L. Barra, C. Sangregorio, R. Sessoli and D. Gatteschi, *Phys. Chem. Chem. Phys.*, 2009
DOI: 10.1039/b905880j

Communication

Radiofrequency polarization effects in zero-field electron paramagnetic resonance
Christopher T. Rodgers, C. J. Wedge, Stuart A. Norman, Philipp Kukura, Karen Nelson, Neville Baker, Kiminori Maeda, Kevin B. Henbest, P. J. Hore and C. R. Timmel, *Phys. Chem. Chem. Phys.*, 2009
DOI: 10.1039/b906102a

Papers

Radiofrequency polarization effects in low-field electron paramagnetic resonance
C. J. Wedge, Christopher T. Rodgers, Stuart A. Norman, Neville Baker, Kiminori Maeda, Kevin B. Henbest, C. R. Timmel and P. J. Hore, *Phys. Chem. Chem. Phys.*, 2009
DOI: 10.1039/b907915g

Three-spin correlations in double electron–electron resonance
Gunnar Jeschke, Muhammad Sajid, Miriam Schulte and Adelheid Godt, *Phys. Chem. Chem. Phys.*, 2009
DOI: 10.1039/b905724b

^{14}N HYSCORE investigation of the H-cluster of [FeFe] hydrogenase: evidence for a nitrogen in the dithiol bridge
Alexey Silakov, Brian Wenk, Eduard Reijerse and Wolfgang Lubitz, *Phys. Chem. Chem. Phys.*, 2009
DOI: 10.1039/b905841a

Tyrosyl radicals in proteins: a comparison of empirical and density functional calculated EPR parameters
Dimitri A. Svistunenko and Garth A. Jones, *Phys. Chem. Chem. Phys.*, 2009
DOI: 10.1039/b905522c

General and efficient simulation of pulse EPR spectra
Stefan Stoll and R. David Britt, *Phys. Chem. Chem. Phys.*, 2009
DOI: 10.1039/b907277b

Dynamic nuclear polarization coupling factors calculated from molecular dynamics simulations of a nitroxide radical in water
Deniz Sezer, M. J. Prandolini and Thomas F. Prisner, *Phys. Chem. Chem. Phys.*, 2009
DOI: 10.1039/b905709a

Dynamic nuclear polarization of water by a nitroxide radical: rigorous treatment of the electron spin saturation and comparison with experiments at 9.2 Tesla
Deniz Sezer, Marat Gafurov, M. J. Prandolini, Vasyl P. Denysenkov and Thomas F. Prisner, *Phys. Chem. Chem. Phys.*, 2009
DOI: 10.1039/b906719c

Dynamic mixing processes in spin triads of "breathing crystals" Cu(hfac)$_2$L^R: a multifrequency EPR study at 34, 122 and 244 GHz
Matvey V. Fedin, Sergey L. Veber, Galina V. Romanenko, Victor I. Ovcharenko, Renad Z. Sagdeev, Gudrun Klihm, Edward Reijerse, Wolfgang Lubitz and Elena G. Bagryanskaya, *Phys. Chem. Chem. Phys.*, 2009
DOI: 10.1039/b906007c

Nitrogen oxide reaction with six-atom silver clusters supported on LTA zeolite
Amgalanbaatar Baldansuren, Rüdiger-A. Eichel and Emil Roduner, *Phys. Chem. Chem. Phys.*, 2009
DOI: 10.1039/b903870a

Multifrequency ESR study of spin-labeled molecules in inclusion compounds with cyclodextrins
Boris Dzikovski, Dmitriy Tipikin, Vsevolod Livshits, Keith Earle and Jack Freed, *Phys. Chem. Chem. Phys.*, 2009
DOI: 10.1039/b903490k

ESR imaging in solid phase down to sub-micron resolution: methodology and applications
Aharon Blank, Ekaterina Suhovoy, Revital Halevy, Lazar Shtirberg and Wolfgang Harneit, *Phys. Chem. Chem. Phys.*, 2009
DOI: 10.1039/b905943a

Multifrequency EPR study of the mobility of nitroxides in solid-state calixarene nanocapsules
Elena G. Bagryanskaya, Dmitriy N. Polovyanenko, Matvey V. Fedin, Leonid Kulik, Alexander Schnegg, Anton Savitsky, Klaus Möbius, Anthony W. Coleman, Gennady S. Ananchenko and John A. Ripmeester, *Phys. Chem. Chem. Phys.*, 2009
DOI: 10.1039/b906827a

Ferro- and antiferromagnetic exchange coupling constants in PELDOR spectra
D. Margraf, P. Cekan, T. F. Prisner, S. Th. Sigurdsson and O. Schiemann, *Phys. Chem. Chem. Phys.*, 2009
DOI: 10.1039/b905524j

Electronic structure of the tyrosine D radical and the water-splitting complex from pulsed ENDOR spectroscopy on photosystem II single crystals
Christian Teutloff, Susanne Pudollek, Sven Keßen, Matthias Broser, Athina Zouni and Robert Bittl, *Phys. Chem. Chem. Phys.*, 2009
DOI: 10.1039/b908093g

A W-band pulsed EPR/ENDOR study of $Co^{II}S_4$ coordination in the $Co[(SPPh_2)(SP^iPr_2)N]_2$ complex
Silvia Sottini, Guinevere Mathies, Peter Gast, Dimitrios Maganas, Panayotis Kyritsis and Edgar J.J. Groenen, *Phys. Chem. Chem. Phys.*, 2009
DOI: 10.1039/b905726a

Exchangeable oxygens in the vicinity of the molybdenum center of the high-pH form of sulfite oxidase and sulfite dehydrogenase
Andrei V. Astashkin, Eric L. Klein, Dmitry Ganyushin, Kayunta Johnson-Winters, Frank Neese, Ulrike Kappler and John H. Enemark, *Phys. Chem. Chem. Phys.*, 2009
DOI: 10.1039/b907029j

Magnetic quantum tunneling: key insights from multi-dimensional high-field EPR
J. Lawrence, E.-C. Yang, D. N. Hendrickson and S. Hill, *Phys. Chem. Chem. Phys.*, 2009
DOI: 10.1039/b908460f

Spin-dynamics of the spin-correlated radical pair in photosystem I. Pulsed time-resolved EPR at high magnetic field
O. G. Poluektov, S. V. Paschenko and L. M. Utschig, *Phys. Chem. Chem. Phys.*, 2009
DOI: 10.1039/b906521k

Enantioselective binding of structural epoxide isomers by a chiral vanadyl salen complex: a pulsed EPR, cw-ENDOR and DFT investigation
Damien M. Murphy, Ian A. Fallis, Emma Carter, David J. Willock, James Landon, Sabine Van Doorslaer and Evi Vinck, *Phys. Chem. Chem. Phys.*, 2009
DOI: 10.1039/b907807j

Topology of the amphipathic helices of the colicin A pore-forming domain in *E. coli* lipid membranes studied by pulse EPR
Sabine Böhme, Pulagam V. L. Padmavathi, Julia Holterhues, Fatiha Ouchni, Johann P. Klare and Heinz-Jürgen Steinhoff, *Phys. Chem. Chem. Phys.*, 2009
DOI: 10.1039/b907117m

Structural characterization of a highly active superoxide-dismutase mimic
Vimalkumar Balasubramanian, Maria Ezhevskaya, Hans Moons, Markus Neuburger, Carol Cristescu, Sabine Van Doorslaer and Cornelia Palivan, *Phys. Chem. Chem. Phys.*, 2009
DOI: 10.1039/b905593b

Structure of the oxygen-evolving complex of photosystem II: information on the S_2 state through quantum chemical calculation of its magnetic properties
Dimitrios A. Pantazis, Maylis Orio, Taras Petrenko, Samir Zein, Wolfgang Lubitz, Johannes Messinger and Frank Neese, *Phys. Chem. Chem. Phys.*, 2009
DOI: 10.1039/b907038a

Population transfer for signal enhancement in pulsed EPR experiments on half integer high spin systems
Ilia Kaminker, Alexey Potapov, Akiva Feintuch, Shimon Vega and Daniella Goldfarb, *Phys. Chem. Chem. Phys.*, 2009
DOI: 10.1039/b906177k

The reduced [2Fe-2S] clusters in adrenodoxin and *Arthrospira platensis* ferredoxin share spin density with protein nitrogens, probed using 2D ESEEM
Sergei A. Dikanov, Rimma I. Samoilova, Reinhard Kappl, Antony R. Crofts and Jürgen Hüttermann, *Phys. Chem. Chem. Phys.*, 2009
DOI: 10.1039/b904597j

Frequency domain Fourier transform THz-EPR on single molecule magnets using coherent synchrotron radiation
Alexander Schnegg, Jan Behrends, Klaus Lips, Robert Bittl and Karsten Holldack, *Phys. Chem. Chem. Phys.*, 2009
DOI: 10.1039/b905745e

PELDOR study of conformations of double-spin-labeled single- and double-stranded DNA with non-nucleotide inserts
Nikita A. Kuznetsov, Alexandr D. Milov, Vladimir V. Koval, Rimma I. Samoilova, Yuri A. Grishin, Dmitry G. Knorre, Yuri D. Tsvetkov, Olga S. Fedorova and Sergei A. Dzuba, *Phys. Chem. Chem. Phys.*, 2009
DOI: 10.1039/b904873a

Site-specific dynamic nuclear polarization of hydration water as a generally applicable approach to monitor protein aggregation
Anna Pavlova, Evan R. McCarney, Dylan W. Peterson, Frederick W. Dahlquist, John Lew and Songi Han, *Phys. Chem. Chem. Phys.*, 2009
DOI: 10.1039/b906101k

Structural information from orientationally selective DEER spectroscopy
J. E. Lovett, A. M. Bowen, C. R. Timmel, M. W. Jones, J. R. Dilworth, D. Caprotti, S. G. Bell, L. L. Wong and J. Harmer, *Phys. Chem. Chem. Phys.*, 2009
DOI: 10.1039/b907010a

Structure and bonding of $[V^{IV}O(acac)_2]$ on the surface of AlF_3 as studied by pulsed electron nuclear double resonance and hyperfine sublevel correlation spectroscopy
Vijayasarathi Nagarajan, Barbara Müller, Oksana Storcheva, Klaus Köhler and Andreas Pöppl, *Phys. Chem. Chem. Phys.*, 2009
DOI: 10.1039/b903826b

Local variations in defect polarization and covalent bonding in ferroelectric Cu2+-doped PZT and KNN functional ceramics at themorphotropic phase boundary
Rüdiger-A. Eichel, Ebru Erünal, Michael D. Drahus, Donald M. Smyth, Johan van Tol, Jérôme Acker, Hans Kungl and Michael J. Hoffmann, *Phys. Chem. Chem. Phys.*, 2009
DOI: 10.1039/b905642d

ESR imaging in solid phase down to sub-micron resolution: methodology and applications

Aharon Blank,*[a] Ekaterina Suhovoy,[a] Revital Halevy,[a] Lazar Shtirberg[a] and Wolfgang Harneit[b]

Received 25th March 2009, Accepted 1st June 2009
First published as an Advance Article on the web 1st July 2009
DOI: 10.1039/b905943a

Electron spin resonance microcopy (ESRM) is an imaging method aimed at the observation of paramagnetic species in small samples with micron-scale spatial resolution. At present, this technique is pursued mainly for biological applications at room temperature and in relatively low static magnetic fields. This work is focused on the use of ESRM for the measurement of solid samples. First, a brief comparison of various electron spin resonance (ESR) detection techniques is provided, with an emphasis on conventional "induction detection". Following that, some methodological details are provided along with experimental examples carried out at room temperature and in a static field of $\sim$0.5 T. These examples show for the first time the imaging of solid samples measured by "induction detection" ESR with a resolution better than 1 μm. Based on these experimental examples and capabilities, an outlook for the future prospects of this methodology in terms of spin sensitivity and resolution is provided. It is estimated that single-spin sensitivity could be achieved for some samples at liquid-helium temperatures and static fields of $\sim$2 T. Furthermore, under these conditions, spatial resolution could reach the nanometer scale. Finally, a description of possible applications of this new methodology is provided.

Introduction

Electron spin resonance microscopy (ESRM) and ESR nanoscopy are a variety of detection and imaging methodologies aimed at obtaining ESR signals from heterogeneous samples with a resolution in the micro- and nano-scales. These techniques have attracted considerable interest in the last few years, demonstrating resolution improvements from a few microns down to the nanometer scale and achieving single-electron-spin sensitivity. For example, scanning tunneling microscopy ESR (STM-ESR),[1,2] which combines the high spatial resolution of STM with the electronic spin sensitivity of ESR, can measure the signal from a single spin with $\sim$1 nm 2D resolution. Magnetic resonance force microscopy (MRFM),[3] which detects the force inflicted by the spins on a sharp magnetic tip demonstrated a single-electron-spin detection capability and 2D imaging with 90 nm resolution.[4] Other methods are not yet that sensitive, or are directed to the measurement of very unique spin systems, but have a potential for improvement in the near future. They include, for example, Hall detection,[5,6] superconducting quantum interference device (SQUID) detection,[7,8] optically detected MR,[9] quantum dot spin detection,[10] single-molecule quantum transport,[11] electrically detected magnetic resonance[12–14] and indirect detection *via* diamond nitrogen-vacancy (NV) centers.[15–17]

While these new methods are very successful and undoubtedly could improve even more in the future, our current approach to high-resolution ESR imaging relies on the more conventional so-called "induction" or "Faraday" detection method. This is because close inspection of the variety of methods presented above reveals some of their inherent limitations and thus, in many ways, they can be considered only as complementary to "induction" detection. For example, STM-ESR works well only under a high vacuum and low temperatures and requires samples deposited on a conductive surface. Furthermore, it cannot provide 3D imaging and it obtains the image in an inefficient manner by scanning the surface point-by-point. The MRFM technique also operates efficiently only at low cryogenic temperatures and under a high vacuum. It has very limited spectroscopic capabilities due to the extreme gradients generated by the magnetic tip used for detection, and cannot be applied in conjunction with modern pulse techniques. Furthermore, MRFM offers only a limited 3D imaging capability since its sensitivity degrades quickly as the distance between the magnetic tip and the sample increases, and it also allows only sequential ("single point") readout of information as the tip scans the sample. Both detection and imaging using Hall probes suffer from substantial degradation as the frequency is elevated (thus limiting its spectroscopic capability) and as the distance from the probe is increased. Furthermore, the sensitivity of Hall probes is strongly dependent on the operating temperature. Another new method of interest is based on indirect spin detection by NV centers; it measures the spins' signal through their dipolar coupling to a single nitrogen vacancy center in a diamond (that can be optically detected). This method has the potential of providing MRFM-like sensitivity and resolution at ambient conditions, but currently it is still very far from that experimental capability and is also inherently limited by the same

[a] *Schulich Faculty of Chemistry, Technion – Israel Institute of Technology, Haifa, 32000, Israel. E-mail: ab359@tx.technion.ac.il; Fax: +972 (0)4 829 5948; Tel: +972 (0)4 829 3679*
[b] *Institut für Experimentalphysik, Freie Universität Berlin, Arnimallee 14, 14195 Berlin, Germany*

problems as MRFM regarding 3D imaging capabilities and spectroscopy. Furthermore, indirect spin detection *via* NV centers could be pursued efficiently only with optically transparent, or at least non-fluorescing (either naturally or photobleached), samples. Table 1 summarizes the current available literature information and provides details related to sensitivity, resolution, operating conditions and 2D/3D imaging capabilities of the methods described above, including "induction detection".

It can be concluded that despite the many new ideas and the vast activity in the field, induction detection remains the only general-purpose approach available today for both spectroscopy and imaging applications. In view of this, we have chosen a route that calls for concentrated efforts improving the capability of induction detection to provide enhanced sensitivity and resolution. Here we will describe our recent efforts in induction detection ESRM of solid samples, which are most suitable to high sensitivity/high resolution measurements. The current measurements were carried out at room temperature and in modest static magnetic fields. Based on these experimental examples and capabilities, an outlook for the future prospects of this methodology in terms the signal-to-noise-ratio (SNR) and resolution achievable at lower temperatures and high static fields, is provided. Finally, a list of possible applications of this technique, relevant to solid samples is presented.

Experimental details

The pulsed ESRM system is based on a "home-built" set that includes a spectrometer, a micro-imaging probe, gradient current drivers and control software. A block diagram of the system is presented in Fig. 1, and its detailed description is provided elsewhere.[18] Briefly, the system is constructed from the following main components: (a) A PC that supervises the image acquisition process and is equipped with four PCI cards with the following functionalities: (b) A timing card with time resolution of 2.5 ns and a minimum pulse length of 2.5 ns. This card generates control signals for the microwave (MW) and gradient pulses of the imaging sequence (Fig. 2), and also for the phases of the transmitted pulses. (c) An 8-bit two-channel digitizer card that acquires the raw ESR data signal, digitizes

Table 1 Comparison of various ESR detection and micro-imaging methods. The first column describes the method of detection/imaging employed. The second column presents the electron spin sensitivity of the method for a relatively long acquisition time (from a few minutes up to ~1 h), as obtained by current state-of-the-art experimental results (in parentheses – the expected sensitivity following near-future methodological developments). The third column shows the current experimental imaging resolution (in parentheses – the expected resolution following near-future methodological developments). The fourth column shows the required measurement conditions in terms of temperature and pressure required to support the sensitivity and resolution specified in columns 2 and 3. The fifth column relates to the issue of sample preparation, a "✓" being granted to methods that do not require a special and elaborate sample preparation as a precondition for measurements. The sixth column considers the method's capabilities in terms of 2D or 3D imaging and how its sensitivity depends upon the sample–probe distance: a method is considered here to be "2D+" if it is inherently 3D, but the signal degrades very quickly as a function of distance from the probe (limiting its actual 3D capability). The seventh column relates to the method's spectroscopic capability. A ✓ is granted to a method which can be used in conjunction with advanced pulsed techniques. A ✓– or ✓? is granted to a method with limited or unknown spectroscopic capabilities. The eighth column describes the method's capability to look at a variety of samples and not be confined to very special samples. A ✓ is granted to a method that can be used for most types of samples. A ✓– is granted to a method that is useful for a relatively limited set of samples

Method	Spin sensitivity	Resolution/μm	Temperature; pressure	Sample preparation	2D or 3D?; distance dependency	Spectroscopy	Not special samples?
Induction, RT[a]	$\sim 3 \times 10^6$ ($\sim 10^5$)	~1 (~0.3)	Ambient; ambient	✓	3D; no dependency	✓	✓
MRFM[b]	<1	~ 0.09 (?)	Low; low	—	2D+; r^{-3} up to r^{-4}	✓–	✓–
SQUID[c]	~30 (~3)	3, 0.2 with lower sensitivity (?)	Low; ambient	✓	2D+; r^{-3}	✓–	✓
Hall, RT[d]	$\sim 10^{13}$ ($\sim 10^8$)	~10 (0.5)	Ambient; ambient	✓	2D+; r^{-3}	✓–	✓
STM-ESR[e]	1	<1 nm	Low; low	—	2D	✓–	✓–
ODMR (NV) Indirect[f]	? (?)	~20 nm	Ambient; ambient	✓	2D+; r^{-3}	✓?	✓
Semiconductor QD, electrical, quantum transport[g]	1–100	NA	Low; ambient	—	NA	✓–	—
Hall, LT[h]	(?)	(?)	Low; ambient	✓	2D+; r^{-3}	✓–	✓
Induction, LT[i]	$\sim 10^8$–10^9 (~1–100)	(~0.01)	Low; ambient	✓	3D; no dependency	✓	✓

[a] Induction detection at room temperature. See ref. 20, 25, 35, 53 and the work presented in this manuscript. [b] See ref. 54 for an updated and detailed account of current and future MRFM capabilities. [c] See ref. 8, 55, 56. [d] See ref. 5. [e] See ref. 5, 57. [f] See ref. 15–17. This recent method detects the fluorescence signal of a specific paramagnetic defect in diamond (NV center) and based on the frequency of the fluorescence, can detect minute magnetic fields. It has not yet actually demonstrated the experimental detection of an ESR signal of a sample external to a nano-diamond placed on an AFM tip (till now, only electron spins in the diamond were detected with this method[58]). Theoretically it holds great promise but issues such as short relaxation times for shallow NV defect centers, and sample self fluorescence signal must be solved prior to achieving high spin sensitivity and image resolution with this tip scanning method. [g] These detection methods are relevant only to unique samples such as semiconductor quantum dots or electrical detection of samples connected to electrodes or placed between two metal layers. The spin sensitivity depends on the exact method pursued. See ref. 10–14, 59. [h] Low-temperature Hall probe detection of magnetic resonance has been suggested as a future method[5] and shows good potential,[60,61] but has not been demonstrated yet. [i] Low-temperature induction detection has yet to be employed in ESR microscopy and the data is based on the analysis presented in this publication. Spin sensitivity in current low-temperature ESR measurements is based on ref. 62.

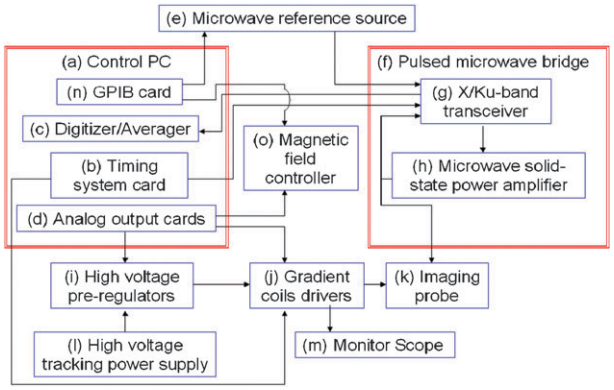

Fig. 1 A block diagram of a typical pulsed ESR micro-imaging system.

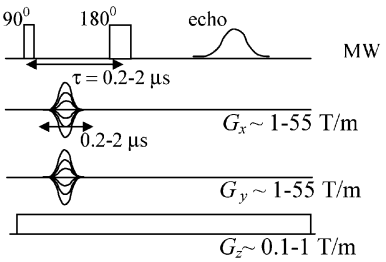

Fig. 2 Typical ESR pulse sequence used for micro-imaging. A simple Hahn echo with a pulse separation of τ, two phase gradients in the *X*- and *Y*-axes, and a constant read gradient along the *Z*-axis.

and averages it according to the user's requirements. (d) An analog output card that generates analog voltages to determine the magnitude of the various gradients in use and controls the static magnetic field *via* the magnetic field controller (o). (n) A GPIB card that controls the functionality of the microwave source and the magnetic field controller. In addition to the PC control software and its attached PCI cards, the system includes the following components: (e) a microwave reference source with a power output of 10 dBm in the 2–18 GHz range; (f) a "home-built" pulsed microwave bridge containing (g) a 6–18 GHz low power transceiver and (h) a solid-state power amplifier with 1 W output, 35 dB gain (home made); The phases of the transmitted pulses from this bridge are digitally controlled by the timing card and can be varied in less than 20 ns. (i) High voltage pre-regulated power supplies for the (j) gradient coil drivers, which provide current drives to the pulsed gradient coils in the imaging probe. The last but probably the most important component in the system, which facilitates its high sensitivity and resolution, is the micro-imaging probe (k). This probe was recently upgraded and therefore is presented here in detail.

Fig. 3 shows a photo and a schematic drawing of the imaging probe. The main philosophy behind our design is to try to minimize the resonator as much as possible and thereby maximize the filling factor of a small sample and also enable the generation of strong gradients by having miniature coils that are very close to the sample.[19] The probe is based on a single ring resonator machined from a TiO_2 (rutile) single crystal. The permittivity of this crystal is anisotropic with values of 165 and 85 (at room temperature) for the field directions that are parallel and perpendicular to the crystal "*C*-axis", respectively.[20] The resonator is constructed from a flat piece in which the *C*-axis of the crystal is in the plane of the resonator ring (see Fig. 4), resulting in an average permittivity of $\sim$125. The resonator operates at $\sim$17 GHz and thus its o.d. is 2.4 mm, its i.d. is 0.9 mm and its height is 0.5 mm. It is excited by a loop at the end of a thin (0.4 mm o.d.) semi-rigid coaxial transmission line. The excitation geometry and the calculated fields for such resonator at the resonance frequency (CST Microwave Studio) are shown in Fig. 4.

The "effective volume" of the resonator[19] can be calculated from the magnetic field distribution and was found to be 1.34 mm^3. The resonator ring and the flat sample are held by a low microwave loss cross-linked polystyrene (Rexolite) piece at an exact position with respect to each other and at the center of the gradient coils' structure. Variable coupling is achieved by changing the distance in two different axes between the resonator ring and the coupling loop at the end of the coaxial MW feed using two linear 1D non-magnetic stages. The third axis, which corresponds to the vertical position of the excitation loop with respect to the resonator ring, can be varied slightly by bending the coaxial line. This variability enables optimal control of the resonator ring's coupling for a wide variety of samples.

The resonator is surrounded by a thin (4.2 mm i.d., 4.6 mm o.d.) quartz tube with 1 μm of gold deposited on it. The gold shields the resonator at the microwave frequencies, but it is transparent to the pulsed magnetic field gradients whose spectral range reaches a maximum of only $\sim$10 MHz (for 100 ns pulses). This kind of structure enables one to maintain a relatively high quality (*Q*)-factor (typically $\sim$1000) for the resonator, even for gradient coils that are in close proximity to it. The *X*-, *Y*-, and *Z*-gradient coils are arranged around the cylindrical shield, along with the regular modulation coils (see Fig. 3b,d). The structure of the *X*-gradient coil is a simple Maxwell pair: the coils of the pair are connected in parallel and have a total inductance of 1.1 μH, a resistance of 0.5 Ω, and produce magnetic field gradient of 1.37 T m^{-1} A^{-1} (calculated *via* the method described in ref. 21). The *Y*-gradient coil is based on Golay geometry: it has a total inductance of 2.09 μH, a resistance of 0.55 Ohm, and it produces magnetic gradient of 1.25 T m^{-1} A^{-1}. Both the X- and Y-gradient coils are driven by the fast pulse current drivers. The *Z*-gradient coil is also based on Golay geometry and has an efficiency of 1.31 T m^{-1} A^{-1}. It has a total inductance of 8.9 μH and a resistance of 1.8 Ω, making it more suitable for static gradient rather than pulsed operation (as required by the imaging sequence Fig. 2). The maximum magnetic field gradient achieved by this system (for the *X* and *Y* coils) with short (0.5–1 μs) current pulses of 40 A (coming out of a 620 V source) is $\sim$55 T m^{-1} with a repetition rate of $\sim$20–40 kHz. One of the major problems of generating such strong gradients at such high-repetition rate is the excessive heat generated in the coils. In order to prevent this problem, the coils are embedded in a heat-conducting (but electrical isolator) adhesive ("Arctic Alumina" with heat conductivity $>$4 W m^{-1} K^{-1}, from Arctic Silver, USA) that is in contact with a brass heat sink (Fig. 3). Furthermore, continuous air flow is applied to the heat sink and into the resonator shield, to

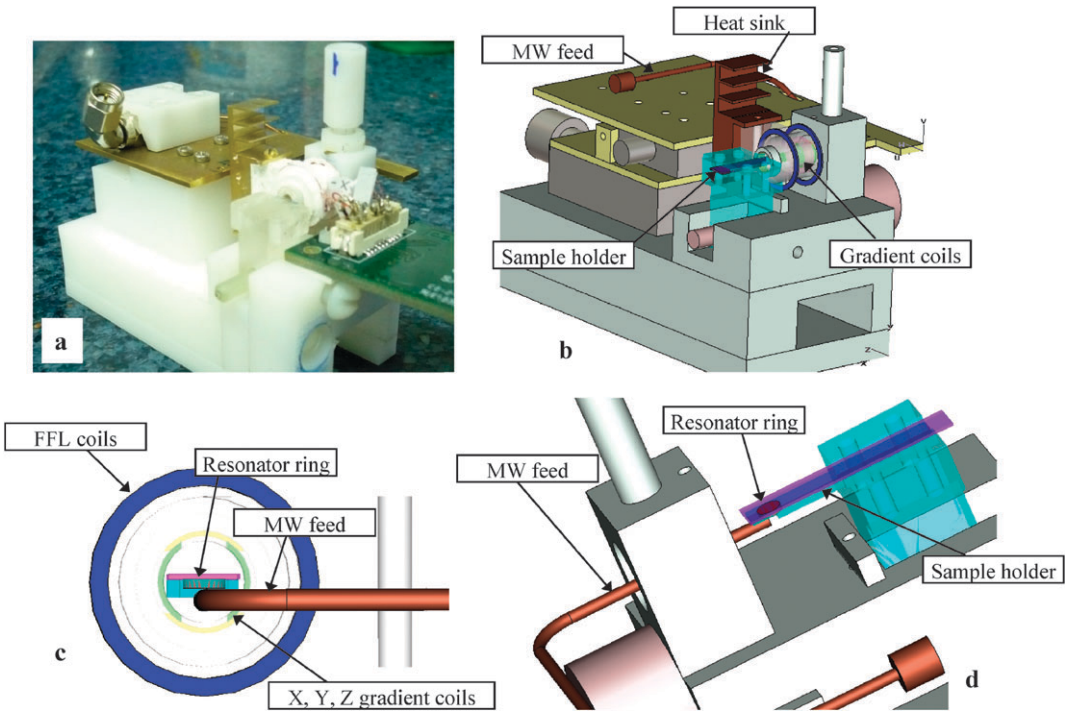

Fig. 3 The structure of the pulsed ESRM probe. (a) A photo of the probe. (b) A schematic drawing of the probe showing an isometric view. (c) A side look of the probe showing the microwave feed, the resonator and the gradient coils located on a cylindrical shield around the resonator. (d) An isometric view of the resonator, sample and microwave feed without the gradient coils.

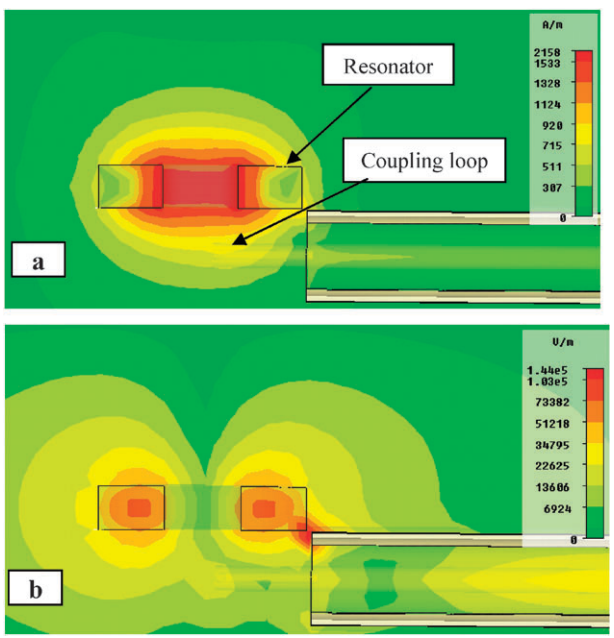

Fig. 4 Calculated magnetic (a) and electric (b) field distribution around the single-ring dielectric resonator inside the cylindrical shield at 17 GHz. The *C*-axis of the rutile single crystal is perpendicular to the plane of the Figure. The magnetic field is maximal at the center of the resonator while the electrical field has a node at the center of the resonator.

maximize heat dissipation and maintain a constant temperature of operation. This efficient heat-removal mechanism is also important for maintaining a fixed resonance frequency for the rutile resonator that can drift by ~10 MHz per K (when operating around 17 GHz[20]). The imaging probe can accommodate flat cylindrical samples with a diameter of ~1 mm (corresponding to the active area/volume of the probe, see Fig. 4) and a height of ~0.5–1 mm. In most cases, samples are placed in a special quartz sample holder that is produced *via* a photolithography technique.[22] If necessary, the samples can be sealed under an argon atmosphere using UV-curable glue (NOA 63 from Norland, USA). This allows the measurement of liquid and solid samples under de-oxygenated conditions as well as positioning the samples in an optimal location inside the resonator without a significant decrease in the resonator's Q.

Results

The pulsed ESRM system described above was employed to obtain the following experimental results with solid samples at room temperature.

i. High-resolution images of LiPc crystals

Single crystals of lithium phthalocyanine (LiPc) represent an almost ideal sample for high-resolution ESR imaging. They have a relatively high spin concentration of 10^8 spins per $[1\ \mu m]^3$,[19,23] and relatively long and almost equal $T_1 = 3.5$ and $T_2 = 2.5\ \mu s$.[24] Furthermore, being solid, they can be measured for relatively long periods of time without changes/movements and they have a negligible effect on the resonator's Q. For that reason, LiPc crystals were used in the past for demonstrating the sensitivity and resolution limits of induction-detection ESR micro-imaging, with the most recent results (prior to this work) achieving a resolution of

$\sim 3 \times 3 \times 8$ μm.[25] In those experiments, the resolution was limited by the strength of the gradient coils, given that single-voxel SNR was more than enough (~ 550). (A voxel is a volume that is the equivalent element to a pixel with a depth component, which is related to slice thickness.) Fig. 5 shows our latest LiPc imaging results carried out with the ESRM system described above. The crystals were prepared by the procedure described in ref. 26. In this measurement we employed the imaging sequence shown in Fig. 2 with $\tau = 1500$ ns, 90° pulse length of 80 ns and 180° pulse length of 180 ns. The gradient half-sine pulses duration were 980 ns for G_x and 1.12 μs for G_y with a maximum current of 40 A (corresponds to ~ 55 T m^{-1}) for G_x and 31 A (corresponds to ~ 39 T m^{-1}) for G_y. This resulted in a maximum gradient-time integral of $\int_t G_x dt = 2.5 \times 10^{-5}$ T s m^{-1} and $\int_t G_y dt = 2.4 \times 10^{-5}$ T s m^{-1} for the X and Y axes, respectively (based on the measured current–time integral multiplied by the calculated gradient efficiency as detailed above). Some of the images (Fig. 5c,d) were obtained without any Z-gradient (pure 2D), while the others (Fig. 5e,f) were recorded with a constant Z-gradient of 0.5 T m^{-1}. The in-plane image resolution was found to be ~ 0.95 and ~ 1.1 μm for the X- and Y- axes respectively. The image resolution was determined by comparing the number of pixels along each axis to the actual physical length of the crystals (for more details regarding the resolution estimation in magnetic resonance microscopy, see ref. 27). The Z-resolution was roughly estimated to be ~ 10–15 μm, based on the estimated height of the crystals. The image acquisition times were 6 and 18 h for the pure 2D and 3D images, respectively (30 and 86 repetitions of individual image acquisition, each with 8 phase cycling steps and

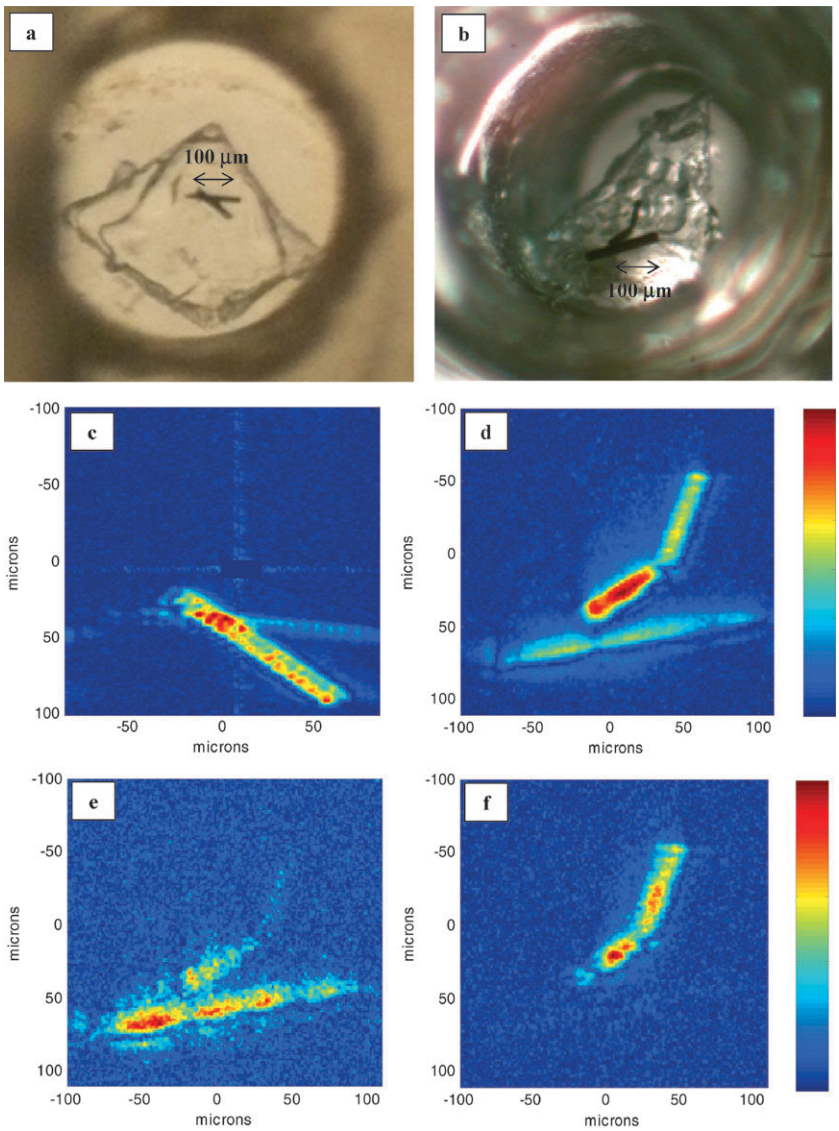

Fig. 5 High-resolution ESR micro-images of LiPc crystals in two test samples. (a) Optical image of the crystals in the first sample. (b) Optical image of the crystals in the second sample. (c) 2D ESR image of the first sample with in plane resolution of $\sim 0.95 \times 1.1$ μm. (d) Same as (c) but for the second sample. (e) 2D slice out of a 3D ESR image of the second sample with in plane resolution of $\sim 0.95 \times 1.1$ μm and slice thickness of ~ 12.5 μm. (f) The same as (e) but for a different 2D slice. The color scale represents the voxel signal intensity in a scale that is normalized to the strongest voxel signal in each image.

220 × 220 k-space steps acquired at coil heat dissipation limited rate of 6 kHz). For this sample the estimated spin concentration is $\sim 10^8$ spins in [1 μm]^3, which results in $\sim 1.3 \times 10^9$ spins per voxel in the 3D image (with a volume of $\sim 0.95 \times 1.1 \times 12.5 = 13$ μm^3). The single voxel SNR was found to be ~24 for the 3D image. Large variations of the signal amplitude between crystal-to-crystal and even within an individual LiPc crystal are evident. The exact origin of these variations was not considered here, although it is well known, for example, that different crystal sizes or different methods of production would result in different T_2 values.

ii. High-resolution images of N@C$_{60}$: C$_{60}$ powder

N@C$_{60}$ is a new class of paramagnetic species[28] with potential applications in a variety of fields ranging from medical imaging[29] to quantum computing.[30] Here we employed this species with a N@C$_{60}$: C$_{60}$ enrichment ratio of ~0.2% both as a test bench for our spectrometer and to show a first step towards the possible application of our methodology in quantum computing. The N@C$_{60}$ powder was produced by the process described in ref. 31. This system's long coherence time makes it very attractive for pulsed ESRM, but its spin concentration (at 0.2% enrichment) is ~3 orders of magnitude smaller than that of LiPc. Larger enrichment factors are possible, but they result in a sharp decrease in T_2, as shall be demonstrated below. Fig. 6 shows a 2D image of the N@C$_{60}$: C$_{60}$ powder mixture placed in a well-defined micro-pattern of letters. The patterns were made by employing standard photolithography technique with SU8-2000 photoresist (from MicroChem) on a thin quartz substrate. In this measurement we employed the imaging sequence shown in Fig. 2 with $\tau = 660$ ns, 90° pulse length of 80 ns and 180° pulse length of 180 ns. The gradient half-sine pulse durations were ~450 ns for G$_x$ and 580 ns for G$_y$ with a maximum current of 16.6 A for G$_x$ and 14.6 A for G$_y$. This resulted in a maximum gradient-time integral of 5.5×10^{-6} T s m^{-1} and 5.6×10^{-6} T s m^{-1} for the X and Y axes, respectively (based on the measured current-time integral multiplied by the calculated gradient efficiency detailed above). No Z-gradient was applied during this acquisition (pure 2D). The image resolution was found to be 4 and 4.6 μm for the X and Y axes, respectively. The image resolution was determined by comparing the number of pixels along each axis to the actual physical length and width of the photolithography prepared letters (see Fig. 6b). The image acquisition time was ~33 h (1760 repetitions of individual image acquisition, each with 8 phase cycling steps and 256 × 200 k-space steps acquired at T_1 limited rate of 6 kHz). For this sample the estimated spin concentration is $\sim 10^5$ spins in [1 μm]^3, which result in $\sim 2.2 \times 10^8$ spins per voxel (with a volume of $4 \times 4.6 \times 120 = 2208$ μm^3). The single voxel SNR was found to be ~16.

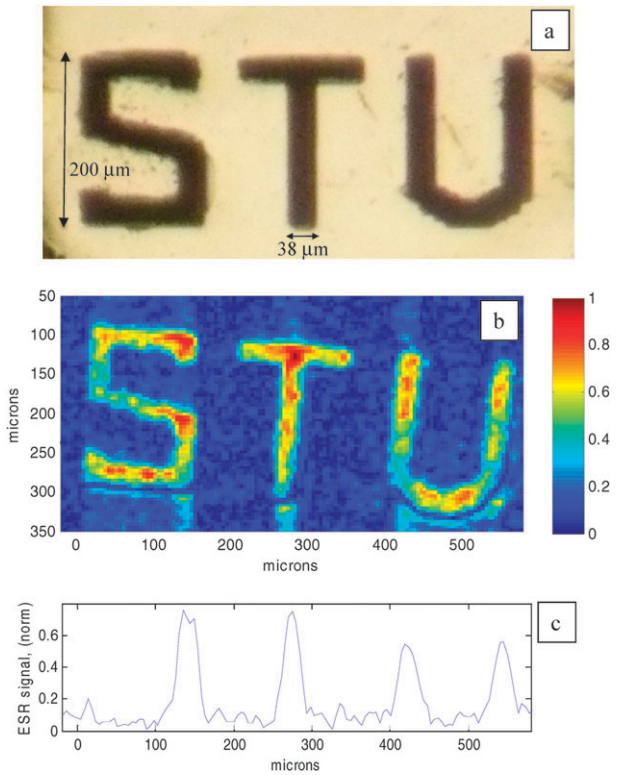

Fig. 6 Optical and ESR images of N@C$_{60}$: C$_{60}$ powder inserted into photolithography-prepared letters. (a) Optical image showing the powder inside the patterns (the lithography thickness is 120 μm). (b) ESR 2D image of the pattern. Here the gradient X-axis of the imaging probe is along the image y-axis (the sample was inserted to the probe with the words written along the Y gradient axis). (c) 1D cut of the ESR image along in the image x-axis (at $y = 225$ microns), showing the level of sharpness of the patterns imaged.

iii. Amplitude and T$_2$ images of N@C$_{60}$: C$_{60}$ powder

As a final example of our ESRM system's current capabilities, a heterogeneous sample of N@C$_{60}$: C$_{60}$ powder with four different levels of enrichment was measured (see Fig. 7). Here we used the imaging sequence shown in Fig. 2 without Z-gradient (pure 2D image), with four different values of τ (500, 800, 1100 and 1400 ns). The 90° pulse length was 80 ns and the 180° pulse length was 180 ns. At each different value of τ an image is acquired and all images are analyzed to obtain the signal amplitude and the T_2 images (Fig. 7b.c), by performing a voxel-wise exponential fit to the data.[25] This is a good example for the capability of the ESRM system to obtain T_2 spatially resolved images of heterogeneous samples. The results clearly show that the higher N@C$_{60}$: C$_{60}$ concentration the larger the single voxel amplitude is (which is obviously expected). Furthermore, for higher N@C$_{60}$: C$_{60}$ concentration shorter T_2 are obtained, due to the increased effect of dipolar interaction. The amplitude of the 0.8% quadrant is a little bit larger than that of the 1.6% quadrant due to larger sample thickness in the former. The T_2 histogram (Fig. 7d) is trimodal with the 1.6% and 0.8% quadrant being very close to each other in terms of their T_2 values. The 2D image resolution is ~20 μm. The gradient half-sine pulses duration were ~250 ns for G$_x$ and 350 ns for G$_y$ with a maximum current of 6.3 A for G$_x$ and 4.9 A for G$_y$ (which are ~50% of the system capability for these gradient pulse lengths).

Discussion and future capabilities

This section compares the results presented above with the theoretical predictions of the SNR and resolution. Based on

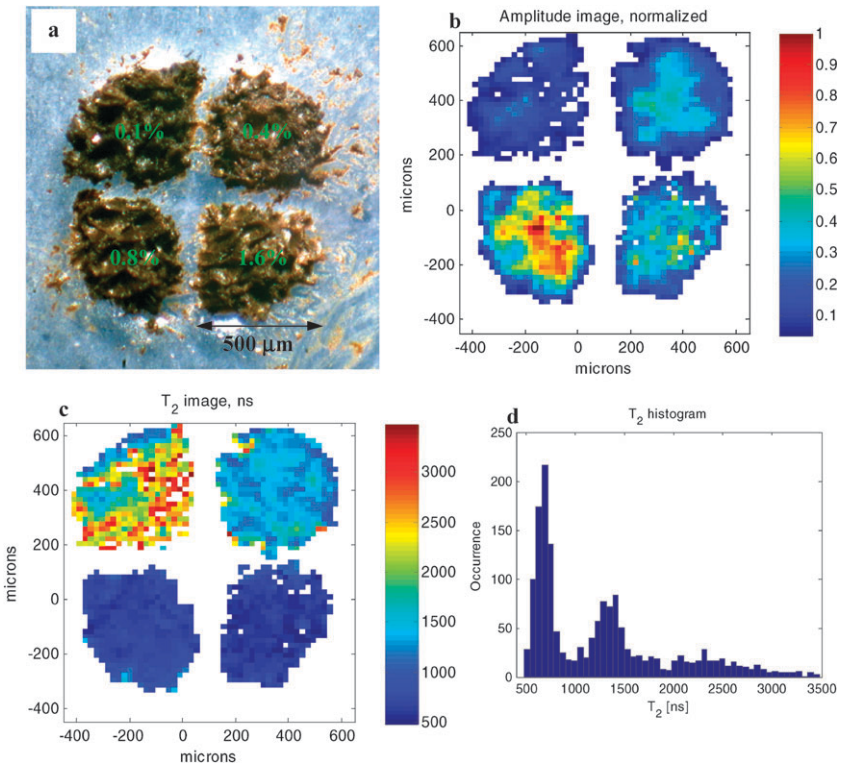

Fig. 7 Amplitude and T_2 images of a heterogeneous sample made of four different types of N@C_{60} : C_{60} powder with N@C_{60} enrichment levels of 0.1, 0.4, 0.8 and 1.6%. (a) Optical image showing the powder grains dispersed in a specially prepared 4 quadrant pattern (by photolithography). (b) ESR amplitude image. (c) ESR T_2 image. (d) Histogram showing the distribution of T_2 vales in the ESR T_2 image.

the current results, this analysis will be extended to predict the future capabilities of induction detection ESRM carried out on solid samples in higher magnetic fields and lower temperatures.

SNR analysis

In general for imaging applications the SNR per voxel can be determined to a good approximation by dividing the SNR of the entire sample by the number of voxels. While the methodology for calculating the free induction decay (FID) or echo signal in nuclear magnetic resonance (NMR) is well-established and validated,[32–34] the situation regarding pulsed ESR requires slight adjustments of the existing formulas. We have recently shown[35] that the single-shot SNR of a small sample with a volume V_v (*e.g.* a single voxel of the image) in a pulsed ESR experiment is given by the expression:

$$\mathrm{SNR}_{\mathrm{pulse}} \approx \frac{\sqrt{2\mu_0}M\omega_0 V_V}{8\sqrt{V_c}\sqrt{k_b T\Delta f}}\sqrt{\frac{Q_u}{\omega_0}} \qquad (1)$$

where M is the specific magnetization of the sample (units of [J T^{-1} m^{-3}]), as given by the Curie law,[36] V_c is the resonator's effective volume,[19] μ_0 is the free space permeability, ω_0 is the Larmor frequency, k_b is the Boltzmann constant, T is the temperature, Δf is the bandwidth of acquisition and Q_u is the unloaded quality factor of the resonator. Eqn (1) assumes that the noise is 4 times larger than the theoretical lower limit and that the resonator's field-power conversion ratio (the amplitude of the B_1 field in the laboratory frame produced by 1 W of excitation MW power) is given by the expression:[37]

$$C_p \approx \sqrt{Q_u\mu_0/2V_c\omega_0} \qquad (2)$$

For one second of acquisition time we can get:

$$\mathrm{SNR}_{\mathrm{pulse}} \approx \frac{\sqrt{2\mu_0}M\omega_0 V_V}{8\sqrt{V_c}\sqrt{k_b T(1/\pi T_2)}}\sqrt{\frac{Q_u}{\omega_0}}\sqrt{\frac{1}{T_1}} \qquad (3)$$

Here we assumed an averaging with a $1/T_1$ repetition rate for SNR improvement and that the bandwidth of excitation is chosen to match the linewidth of the imaged paramagnetic species in the sample, $\Delta f = 1/\pi T_2$.

Resolution analysis

The experiments presented above made use of the simple imaging pulse sequence shown in Fig. 2. Considering this sequence, we can write that for a radical characterized by a Lorentzian lineshape with a width of $1/(\pi T_2)$, the resolution as a function of the constant gradient (G_z in Fig. 2) is given by:[38]

$$\Delta z = 2/\gamma\, G_z T_2 \qquad (4)$$

It should be noted that diffusion of the spins in the solute in the presence of such a constant gradient does not significantly affect the echo amplitude (in contrast to NMR, where the maximum applied gradient is limited by this phenomenon).

This advantage of ESRM is apparent after reviewing the expression: [39]

$$\text{Echo amplitude} = e^{(-\frac{1}{3}\gamma^2 G_z^2 D\tau^3)} \quad (5)$$

which shows that in most cases, for the short time scales of ESR (τ), the reduction in the echo signal amplitude is negligible. For example, employing eqn (5), even with a relatively fast diffusion of $D = 10^{-9}$ m^2 s^{-1}, a very high G_z of 40 T m^{-1} and $\tau = 1$ μs (Fig. 2), results in an echo decay of only ~2%. Thus, it is clear that even with gradients that correspond to sub-micron image resolution there is no significant prohibiting decay due to diffusion. Nevertheless some applications do require the measurement of diffusion or motion in short-time scales (1–100 μs) and this can be performed in ESRM systems by means of a different sequence than the one shown in Fig. 2 (stimulated echo sequence), taking advantage of spin system having a relatively long T_1 with respect to T_2.[40] Such capability was recently demonstrated in our laboratory where direct measurements of the diffusion of paramagnetic species, such as deuterated trityl and N@C_{60}, were performed in liquid solutions.[31]

From the constant Z-gradient, we now turn to the X- and Y-phase gradients (Fig. 2). The resolution in these axes is given by:[39]

$$\Delta x = \frac{1}{(\gamma/2\pi)\int_t G_x \mathrm{d}t} \quad (6)$$

It is clear from this expression that the shape of the phase gradient is not of importance, thereby relaxing the technical constraints for its generation. The parameter T_2 does not appear explicitly in eqn (6). However, since the duration of the gradient pulse should be shorter than τ (Fig. 2), it is clear that, in practice, having a longer T_2 means that one can use longer τ with small reduction of the signal magnitude and thereby use a longer gradient pulse and achieve a better resolution.

Comparison between experimental results and the theoretical predictions

i. High-resolution images of LiPc crystals

Based on the time-gradient integral detailed above and eqn (6), the theoretical resolution is found to be ~1.32 and 1.38 μm for the X- and Y-axes, respectively. The theoretical resolution along the Z axis can be calculated *via* eqn (4) and was found to be ~12.3 μm. Based on eqn (3) the theoretical single voxel SNR (after all the averaging process described above) is found to be ~257, when taking into consideration the sample spin concentration, the resonator unloaded Q_u (~1000), the resonator effective volume, the bandwidth of acquisition for each image slice (0.5 MHz) and the measurement repetition rate.

ii. High-resolution images of N@C_{60} : C_{60} powder

The same formulation can be employed to find the theoretical SNR and resolution for the case of the N@C_{60} : C_{60} powder. Based on the time-gradient detailed above and eqn (6), the theoretical resolution is found to be ~6.5 and 6.4 μm for the X- and Y-axes, respectively. Based on eqn (3) the theoretical single voxel SNR (after all the averaging process described above) is found to be ~43, when taking into consideration the sample spin concentration, the resonator unloaded Q_u (~1000), the resonator effective volume, the bandwidth of acquisition (1 MHz) and the measurement repetition rate.

It can be concluded that in the two different types of test samples we employed here (LiPc and N@C_{60}) the theoretical resolution was found to be a bit lower than the actual measured values. This is probably due to our calculations of the gradient coils efficiency (in T m^{-1} A^{-1}) that are a bit too conservative (see the probe description in the experimental section above). As for the single voxel SNR, it was found to be somewhat lower than the expected values, however due to the large uncertainty in the spin concentration of the samples and its large variations inside the sample (for example from one LiPc crystal to the other, and inside the crystals), the predictions are in reasonable agreement to theory.

Future possibilities for "induction detection" ESR and ESRM

As shown above, the experimental results are in adequate agreement with the theoretical analysis of SNR and image resolution. While the current results presented here constitute the "state-of-the-art" in terms of sensitivity and resolution for induction detection ESR, there is clearly much room for improvement by going to higher fields and lower temperatures. Based on the current experimental and theoretical results we can present a prediction for the SNR and resolution when carrying out ESRM experiments in varying sets of frequencies and temperatures.

SNR as a function of temperature and static magnetic field

The SNR can be calculated using eqn (3), based on the knowledge of parameters such as the resonator's "effective" volume, V_c, unloaded quality factor, Q_u, and the radical T_1 and T_2. Assuming one employs a dielectric ring resonator of the type presented here (see Fig. 3,4), the "effective" volume for a given frequency can be calculated on the basis of the crystal's permittivity. A typical dielectric resonator has an outer radius, a, that is ~2.5 times larger than its height. Thus, for a crystal with relative permittivity, ε_r, the radius can be calculated by the expression:[41]

$$a \approx \frac{202}{f\sqrt{\varepsilon_r}} \quad (7)$$

where a is expressed in mm and f in GHz. Since most of the RF magnetic field is concentrated in a radii of $a/2$ (see Fig. 4), the "effective" volume of the resonator can be approximated by the expression:

$$V_c \approx \pi\left(\frac{a}{2}\right)^2\left(\frac{a}{2.5}\right) \approx \frac{7.8\times 10^6}{f^3\varepsilon_r^{3/2}} \quad (8)$$

This equation accounts for the fact that, although most of the magnetic field is "confined" to a radius of $a/2$ and a height of $a/2.5$, there is still a considerable amount of magnetic energy

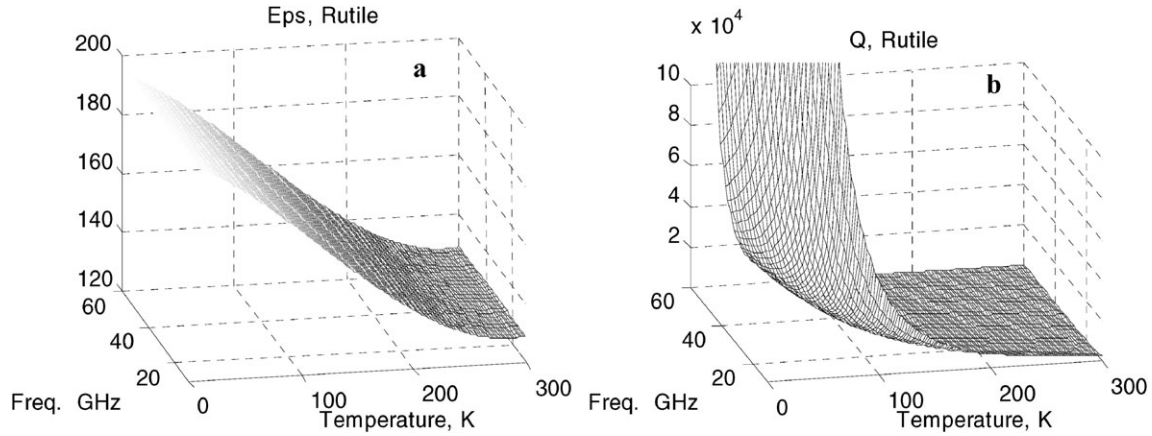

Fig. 8 Single-crystal dielectric properties as a function of frequency and temperature. (a) Rutile crystal, ε. (b) Rutile crystal, Q;

outside this volume, which effectively reduces the filling factor and thus increases the "effective volume" by a factor of ~ 3.[35]

Eqn (3) and (8) can now be used, along with the dielectric properties of the resonators crystals and the relaxation times of the measured spins, to provide an estimate for spin sensitivity as a function of temperature and frequency. Fig. 8 presents the rutile crystal's dielectric properties as a function of temperature and frequency. This data was used to calculate the minimum number of detectable spins per 60 min of acquisition time for a typical sample of LiPc (assuming temperature and field-independent $T_1 = 3.5$ μs and $T_2 = 2.5$ μs). The calculations are presented in Fig. 9. It is evident from Fig. 9 that at high fields and low temperatures one could approach and even surpass single electron spin sensitivity. Above 60 GHz and below 4 K the available information is not reliable enough to allow the extrapolation of the SNR calculations with a reasonable degree of certainty.

Resolution as a function of temperature and static magnetic field

In principle, the SNR calculations that were provided above can be used to immediately obtain the image resolution, based on the sample spin concentration. However, one should also consider the possibilities of generating gradients that are large enough to support the SNR-limited image resolution. We will consider as an example the sample of LiPc crystals that, as was noted above, typically has 10^8 spins per [1 μm]^3. If one achieves single-spin sensitivity then the resolution for this sample could approach, in principle, the 1 nm-scale (sensitivity-wise). However, such high resolution requires also the use of very powerful gradients that are beyond the current state-of-the-art. For example, our existing 17 GHz probe has gradient coils with an efficiency of ~ 1.4 T m^{-1} A^{-1} and our current drivers can produce up to 40 A peak current for a duration of 1.5 μs. The implementation of this information in eqn (6) results in an available theoretical resolution of ~ 700 nm, as was validated by the experimental results presented above. This is still a long way from the SNR-limited 1 nm-scale resolution. In order to estimate how far one can go (resolution-wise), we follow the reasoning of the previous sub-section and consider the implications for the attainable resolution of increasing the magnetic field and/or decreasing the temperature.

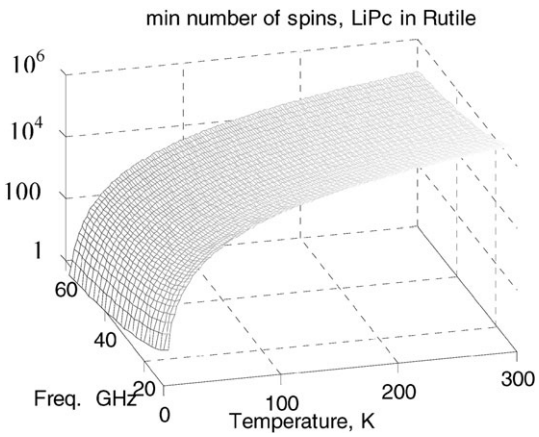

Fig. 9 The minimum number of detectable spins for LiPc sample, 1 h of acquisition time, as a function of frequency and temperature for a rutile resonator.

The gradient coils' efficiency, in T m^{-1} A^{-1}, keeping constant the number of windings in the coil, scales as $1/b^2$, where b is a typical gradient-coil radius,[21] that is about twice the resonator's radius, a (which can be estimated through eqn (7)). Thus, if we take the 17 GHz probe based on a rutile single crystal as a reference (with $b \sim 2.5$ mm at room temperature), we find that at 60 GHz and 4 K the expected gradient coil radius would be $b \sim 0.6$ mm. Such a decrease in coil size immediately translates into a factor of $(2.5/0.6)^2 \sim 17$ in gradient coil efficiency. Furthermore, if we keep the coil inductance and resistance (proportional to b^2 and b, respectively) similar to those of the 17 GHz probe, the number of windings can increase by a factor of ~ 4, meaning an overall increase of a factor of $\sim 17 \times 4 = 68$ in gradient coil efficiency. This means that, with the same current pulse of maximum 40 A and 1.5 μs duration described above, one would obtain a theoretical resolution of $\sim 700/68 \sim 10.3$ nm. Additional foreseeable future upgrades in the gradient current drivers (such as increasing the drive voltage to 1000 V and improving the circuit components) can bring the available current up to ~ 120 A, and with longer gradient pulses of up to 3 μs (for species having long enough T_2), the theoretical resolution would reach ~ 1.7 nm. It should be mentioned, however, that

one of the limiting factors relevant in these extreme cases is the heat dissipated in the gradient coils. As the coils become smaller, heating becomes more of a problem. Possible ways around this problem are either decreasing the acquisition repetition rate (meaning a longer acquisition time to achieve a sufficient SNR), or using superconducting wires as gradient coils (which is relevant only when the measurements are carried out at cryogenic temperatures).

Potential applications

To conclude our presentation of ESRM in solid phase samples it would be worthwhile mentioning some possible applications of this methodology.

1. Imaging of semiconductor devices

Classical semiconductor devices are fabricated in most cases on Si or GaAs substrates using accurate processes such as material etching, deposition and oxygenation. Upon completion, they constitute a complex 3D structure made of substrate crystal, metallic contacts, doped elements, and/or insulators. There is a general need to provide non-invasive high-resolution 3D imaging of these sophisticated structures. Such images can be used to identify the source of failure mechanisms (FA) in newly-designed and newly-fabricated chips, and for quality assurance (QA) purposes on devices in the production line. ESR imaging of semiconductor devices can take advantage of the fact that most of the materials that constitute the device (*e.g.* p-type and n-type silicon, metal contacts and lines and even defects in intrinsic Si or SiO_2) produce good ESR signals, especially at low temperatures.[42] Micro ESR imaging can also be useful in the field of organic semiconductors[43] where it can help one to understand the complex transport/recombination behavior of the charge carriers in these systems as well as doping issues, interface effects and micro-morphology related effects.

2. Imaging of radiation defects

ESR imaging has been used for a long time in dosimetry and in the assessment of radiation damage in bones[44] and tooth enamel.[45] The information obtained by ESR imaging enables one to determine the spatial distribution of the effects caused by radiation, as well as to determine possible inhomogeneities in the imaged structure. Improved spatial resolution would reveal the effects of ionizing radiation on a fine scale, a matter that is of special interest in this research area.[46,47]

3. ESR imaging of chemical reactions in the solid phase

ESR imaging has been used to evaluate polymer degradation,[48,49] to enable *in situ* observation of the spatial distribution of paramagnetic species (such as reactants, products and intermediates) in catalyst systems, to monitor diffusion in a catalyst pellet, and to characterize poisoning in micro fixed-bed reactors.[50] In addition, ESR imaging was used to explore other chemically-related processes such as annealing under a thermal gradient.[51] Again, this line of research is likely to benefit from the availability of an ESR-based microscope with enhanced sensitivity and improved spatial resolution.

4. ESRM for quantum computing

Quantum computation (QC) is a relatively new field of science that is aimed at using the quantum properties of systems such as molecules, electrons and photons in favor of complex calculations. Problems such as the factorization of large numbers or an item search in a large database could be solved much more efficiently by quantum computers than using classical computing devices. Several recent proposals for workable quantum computers are based on the use of paramagnetic species in the solid phase such as $N@C_{60}$[30] or phosphorous doped silicon.[52] High-resolution ESR microscopy with single-spin sensitivity and nm scale resolution would be a very useful tool for manipulating and detecting the spins in such systems.

Acknowledgements

This work was partially supported by the Israeli Science Foundation (grants 169/05 and 1143/05), the BSF foundation (grant 2005258), the European Research Council (ERC grant 201665), and by the Russell Berrie Nanotechnology Institute at the Technion. The help of Yael Talmon with the preparation of photolithographic glass sample holders is also greatly appreciated.

References

1 Y. Manassen, R. J. Hamers, J. E. Demuth and A. J. Castellano, *Phys. Rev. Lett.*, 1989, **62**, 2531–2534.
2 C. Durkan and M. E. Welland, *Appl. Phys. Lett.*, 2002, **80**, 458–460.
3 D. Rugar, R. Budakian, H. J. Mamin and B. W. Chui, *Nature*, 2004, **430**, 329–332.
4 H. J. Mamin, M. Poggio, C. L. Degen and D. Rugar, *Nat. Nanotechnol.*, 2007, **2**, 301–306.
5 G. Boero, P. A. Besse and R. Popovic, *Appl. Phys. Lett.*, 2001, **79**, 1498–1500.
6 P. Kejik, G. Boero, M. Demierre and R. S. Popovic, *Sens. Actuators, A*, 2006, **129**, 212–215.
7 R. McDermott, A. H. Trabesinger, M. Muck, E. L. Hahn, A. Pines and J. Clarke, *Science*, 2002, **295**, 2247–2249.
8 C. I. Pakes, P. W. Josephs-Franks, R. P. Reed, S. G. Corner and M. S. Colclough, *IEEE Trans. Instrum. Meas.*, 2001, **50**, 310–313.
9 J. Wrachtrup, C. von Borczyskowski, J. Bernard, M. Orrit and R. Brown, *Nature*, 1993, **363**, 244–245.
10 J. M. Elzerman, R. Hanson, L. H. W. van Beveren, B. Witkamp, L. M. K. Vandersypen and L. P. Kouwenhoven, *Nature*, 2004, **430**, 431–435.
11 J. E. Grose, E. S. Tam, C. Timm, M. Scheloske, B. Ulgut, J. J. Parks, H. D. Abruna, W. Harneit and D. C. Ralph, *Nat. Mater.*, 2008, **7**, 884–889.
12 W. Harneit, C. Boehme, S. Schaefer, K. Huebener, K. Fostiropoulos and K. Lips, *Phys. Rev. Lett.*, 2007, **98**, 216601.
13 D. R. McCamey, H. Huebl, M. S. Brandt, W. D. Hutchison, J. C. McCallum, R. G. Clark and A. R. Hamilton, *Appl. Phys. Lett.*, 2006, **89**, 182115.
14 A. R. Stegner, C. Boehme, H. Huebl, M. Stutzmann, K. Lips and M. S. Brandt, *Nat. Phys.*, 2006, **2**, 835–838.
15 G. Balasubramanian, I. Y. Chan, R. Kolesov, M. Al-Hmoud, J. Tisler, C. Shin, C. Kim, A. Wojcik, P. R. Hemmer, A. Krueger, T. Hanke, A. Leitenstorfer, R. Bratschitsch, F. Jelezko and J. Wrachtrup, *Nature*, 2008, **455**, 648–U646.
16 J. R. Maze, P. L. Stanwix, J. S. Hodges, S. Hong, J. M. Taylor, P. Cappellaro, L. Jiang, M. V. G. Dutt, E. Togan, A. S. Zibrov, A. Yacoby, R. L. Walsworth and M. D. Lukin, *Nature*, 2008, **455**, 644–U641.

17 J. M. Taylor, P. Cappellaro, L. Childress, L. Jiang, D. Budker, P. R. Hemmer, A. Yacoby, R. Walsworth and M. D. Lukin, *Nat. Phys.*, 2008, **4**, 810–816.
18 E. Suhovoy and A. Blank, *Isr. J. Chem.*, 2008, **48**, 45–51.
19 A. Blank, C. R. Dunnam, P. P. Borbat and J. H. Freed, *J. Magn. Reson.*, 2003, **165**, 116–127.
20 M. E. Tobar, J. Krupka, E. N. Ivanov and R. A. Woode, *J. Appl. Phys.*, 1998, **83**, 1604–1609.
21 J.-M. Jin, *Electromagnetic Analysis and Design in Magnetic Resonance Imaging*, CRC Press, Boca Raton, 1999.
22 R. Halevy, Y. Talmon and A. Blank, *Appl. Magn. Reson.*, 2007, **31**, 591–598.
23 K. J. Liu, G. Bacic, P. J. Hoopes, J. J. Jiang, H. K. Du, L. C. Ou, J. F. Dunn and H. M. Swartz, *Brain Res.*, 1995, **685**, 91–98.
24 J. W. Stoner, D. Szymanski, S. S. Eaton, R. W. Quine, G. A. Rinard and G. R. Eaton, *J. Magn. Reson.*, 2004, **170**, 127–135.
25 A. Blank, J. H. Freed, N. P. Kumar and C. H. Wang, *J. Controlled Release*, 2006, **111**, 174–184.
26 P. Turek, J. J. Andre, A. Giraudeau and J. Simon, *Chem. Phys. Lett.*, 1987, **134**, 471–476.
27 L. Ciobanu, D. A. Seeber and C. H. Pennington, *J. Magn. Reson.*, 2002, **158**, 178–182.
28 T. Almeida Murphy, T. Pawlik, A. Weidinger, M. Hohne, R. Alcala and J. M. Spaeth, *Phys. Rev. Lett.*, 1996, **77**, 1075–1078.
29 Patent application, (WO/2006/116021) *MRI Technique based on Electron Spin Resonance and Endohedral Contrast Agent*, 2006.
30 W. Harneit, C. Meyer, A. Weidinger, D. Suter and J. Twamley, *Phys. Status Solidi B*, 2002, **233**, 453–461.
31 A. Blank, Y. Talmon, M. Shklyar, L. Shtirberg and W. Harneit, *Chem. Phys. Lett.*, 2008, **465**, 147–152.
32 D. I. Hoult and R. E. Richards, *J. Magn. Reson.*, 1976, **24**, 71–85.
33 D. I. Hoult and N. S. Ginsberg, *J. Magn. Reson.*, 2001, **148**, 182–199.
34 J. Jeener and F. Henin, *J. Chem. Phys.*, 2002, **116**, 8036–8047.
35 A. Blank and J. H. Freed, *Isr. J. Chem.*, 2006, **46**, 423–438.
36 G. A. Rinard, R. W. Quine, R. T. Song, G. R. Eaton and S. S. Eaton, *J. Magn. Reson.*, 1999, **140**, 69–83.
37 C. P. Poole, *Electron Spin Resonance: A Comprehensive Treatise on Experimental Techniques*, Wiley, New York, 1983.
38 G. G. Maresch, M. Mehring and S. Emid, *Physica B & C*, 1986, **138**, 261–263.
39 P. T. Callaghan, *Principles of Nuclear Magnetic Resonance Microscopy*, Oxford University Press, Oxford, 1991.
40 T. J. Norwood, *J. Magn. Reson., Ser. A*, 1993, **103**, 258–267.
41 D. Kajfez and P. Guillon, *Dielectric Resonators*, Artech House, Dedham, MA, 1986.
42 T. Umeda, S. Hagiwara, M. Katagiri, N. Mizuochi and J. Isoya, *Phys. B*, 2006, **376–377**, 249–252.
43 M. Wohlgenannt, Z. V. Vardeny, J. Shi, T. L. Francis, X. M. Jiang, O. Mermer, G. Veeraraghavan, D. Wu and Z. H. Xiong, *IEE Proc. Circuits Devices Syst.*, 2005, **152**, 385–392.
44 D. A. Schauer, M. F. Desrosiers, P. Kuppusamy and J. L. Zweier, *Appl. Radiat. Isot.*, 1996, **47**, 1345–1350.
45 S. S. Ishchenko, S. M. Okulov and I. P. Vorona, *Phys. Solid State*, 1999, **41**, 1100–1101.
46 A. A. Romanyukha, M. G. Mitch, Z. C. Lin, V. Nagy and B. M. Coursey, *Radiat. Res.*, 2002, **157**, 341–349.
47 G. A. Watt, M. E. Newton and J. M. Baker, *Diamond Relat. Mater.*, 2001, **10**, 1681–1683.
48 K. Kruczala, M. V. Motyakin and S. Schlick, *J. Phys. Chem. B*, 2000, **104**, 3387–3392.
49 M. Lucarini, G. F. Pedulli, M. V. Motyakin and S. Schlick, *Prog. Polym. Sci.*, 2003, **28**, 331–340.
50 Z. Xiang and Y. Xu, *Appl. Magn. Reson.*, 1997, **12**, 69–79.
51 M. Ikeya and M. Yamamoto, *Jpn. J. Appl. Phys.*, 1994, **33**, L1087–L1089.
52 B. E. Kane, *Nature*, 1998, **393**, 133–137.
53 A. Blank, C. R. Dunnam, P. P. Borbat and J. H. Freed, *Appl. Phys. Lett.*, 2004, **85**, 5430–5432.
54 S. Kuehn, S. A. Hickman and J. A. Marohn, *J. Chem. Phys.*, 2008, **128**, 052208.
55 S. K. H. Lam and D. L. Tilbrook, *Appl. Phys. Lett.*, 2003, **82**, 1078–1080.
56 L. Hao, J. C. Macfarlane, J. C. Gallop, D. Cox, J. Beyer, D. Drung and T. Schurig, *Appl. Phys. Lett.*, 2008, **92**, 192507.
57 M. Mannini, P. Messina, L. Sorace, L. Gorini, M. Fabrizioli, A. Caneschi, Y. Manassen, P. Sigalotti, P. Pittana and D. Gatteschi, *Inorg. Chim. Acta*, 2007, **360**, 3837–3842.
58 T. Gaebel, M. Domhan, I. Popa, C. Wittmann, P. Neumann, F. Jelezko, J. R. Rabeau, N. Stavrias, A. D. Greentree, S. Prawer, J. Meijer, J. Twamley, P. R. Hemmer and J. Wrachtrup, *Nat. Phys.*, 2006, **2**, 408–413.
59 M. Xiao, I. Martin, E. Yablonovitch and H. W. Jiang, *Nature*, 2004, **430**, 435–439.
60 R. B. Dinner, M. R. Beasley and K. A. Moler, *Rev. Sci. Instrum.*, 2005, **76**, 103702.
61 A. K. Geim, S. V. Dubonos, J. G. S. Lok, I. V. Grigorieva, J. C. Maan, L. T. Hansen and P. E. Lindelof, *Appl. Phys. Lett.*, 1997, **71**, 2379–2381.
62 M. Bennati, C. T. Farrar, J. A. Bryant, S. J. Inati, V. Weis, G. J. Gerfen, P. Riggs-Gelasco, J. Stubbe and R. G. Griffin, *J. Magn. Reson.*, 1999, **138**, 232–243.